Single-molecule controlled emission in planar plasmonic cavities

S. Derom,[1] A. Bouhelier,[1] A. Kumar,[1] A. Leray,[2] J-C. Weeber,[1] S. Buil,[3] X. Quélin,[3]
J. P. Hermier,[3,4] and G. Colas des Francs[1,*]

[1]*Laboratoire Interdisciplinaire Carnot de Bourgogne (ICB), UMR 6303 CNRS, Université de Bourgogne, 9 Avenue Savary, BP 47870, 21078 Dijon Cedex, France*

[2]*Institut de Recherche Interdisciplinaire (IRI), USR 3078 CNRS, Université de Lille-Nord de France, BCF, Parc de la Haute Borne, 59650 Villeneuve d'Ascq, France*

[3]*Groupe d'Etude de la Matière Condensée (GEMaC), Université de Versailles-Saint Quentin en Yvelines, CNRS UMR 8635, 45 avenue des Etats-Unis, 78035 Versailles Cedex, France*

[4]*Institut Universitaire de France, 103, Bd Saint-Michel, 75005 Paris, France*

(Received 13 September 2013; published 2 January 2014)

We study the fluorescence emission from single dye molecules in coplanar plasmonic cavities composed of a thin gold film surrounded by two in-plane surface plasmon Bragg mirrors. We first discuss the effect of the presence of Bragg mirrors on the radiation diagram of surface plasmon coupled emission. Then, we investigate the role of the planar cavity size by single-molecule fluorescence lifetime imaging. Experimental data are compared to numerical simulations of the decay rates calculated as a function of the molecule orientation and position within the cavity. The creation of new decay channels by coupling to the cavity modes is also discussed. We measure a plasmonic Purcell factor up to five, attributed to the enhancement of the radiative rate.

DOI: 10.1103/PhysRevB.89.035401 PACS number(s): 42.50.Pq, 73.20.Mf

I. INTRODUCTION

The integration of optical nanosources in microcavities is of key interest for the control and enhancement of light emission. Optical microcavities support strongly confined modes into which the spontaneous emission of a quantum emitter is mainly redirected. Important potential applications in this context are for example the realization of efficient light emitting diodes, low-threshold lasers, and the control of Förster resonant energy transfer (for reviews, see, e.g., Refs. 1 and 2).

Optical microcavities generally rely on 3D confinement of bulk modes to improve light-matter interaction. However, this necessitates realizing for instance complex 3D photonic band gap crystals and leads to challenging nanofabrication processes.[3] Simpler geometries rely on photonic crystal slabs or nanobeam cavities. In that case, a guided wave is confined thanks to Bragg mirrors designed into the guiding structure. The guiding structure confines the wave in the transverse direction(s) whereas the Bragg mirrors ensure confinement along the longitudinal direction. This configuration permits achieving high Q/V ratio cavities integrated on photonic devices, even with poor index contrast (Q and V refer to the mode quality factor and volume, respectively).[4] In addition, the evanescent waves that appear in the near field of the cavity are easily accessible for light manipulation at the nanoscale.[5,6] Another possibility is to confine surface waves such as surface plasmon polaritons (SPPs). A SPP is a collective oscillation of the surface density of charges that propagates along a metal/dielectric interface. It is naturally confined at the metal surface so that a planar constraint is sufficient to achieve a full 3D mode confinement. Moreover, this ensures the possibility for direct coupling to the SPP mode, instead of evanescent coupling to a waveguide mode. Last, the SPP mode field is generally more intense as compared to evanescent waves originating from total internal reflection. In this context, we are interested in planar plasmonic cavities since it is a direct transposition of Fabry-Perot optical microcavities to surface waves. An in-plane plasmonic cavity consists of two SPP distributed Bragg reflectors (DBRs) deposited on a flat metal film.[7–11] The SPP confinement in a planar cavity was demonstrated by near-field optical microscopy[8–10] and cathodoluminescence.[15,16] In addition, the capabilities of SPP cavities for improving solid state optical sources were emphasized by the works of Winter and Barnes[17] and Gonga and Vukovic.[11] Moreover, the integration of an efficient single-photon source into a photonic device is a challenging topic and plasmonic-based elements appear promising in this context thanks to the strong mode confinement.[12–14] In this work, we are interested in the control of single-emitter fluorescence in coplanar plasmonic cavities.

We investigate the fluorescence decay rate of localized fluorescent sources deposited into a planar plasmonic cavity. To this aim, we first discuss in Sec. II the effect of a single SPP Bragg reflector on the propagation of a locally excited plasmon. We notably characterize the efficiency of the mirror at the emission wavelength. We then describe in Sec. III position-sensitive fluorescence lifetime measurements of single dye molecules randomly dispersed in a cavity composed of two DBRs. We show that the dye photodynamics is governed by the surface modes confined in the plasmonic cavity, in direct analogy with the emission control obtained by the confinement of bulk modes in a one-dimensional (1D) Fabry-Perot cavity.

II. SURFACE PLASMON COUPLED EMISSION NEAR A DISTRIBUTED SPP BRAGG MIRROR

Prior to the characterization of single-molecule lifetime within coplanar cavities, we investigate the effect of the presence of a single Bragg mirror onto surface plasmon coupled emission[19,20] (SPCE) of fluorescent nanobeads. Figure 1 represents the optical setup, a schematic view of the sample and a scanning electron micrograph of the Bragg mirror. The SPP Bragg mirror consists of six gold ridges (period Λ, width $W = 90$ nm, and height $h = 50$ nm; see

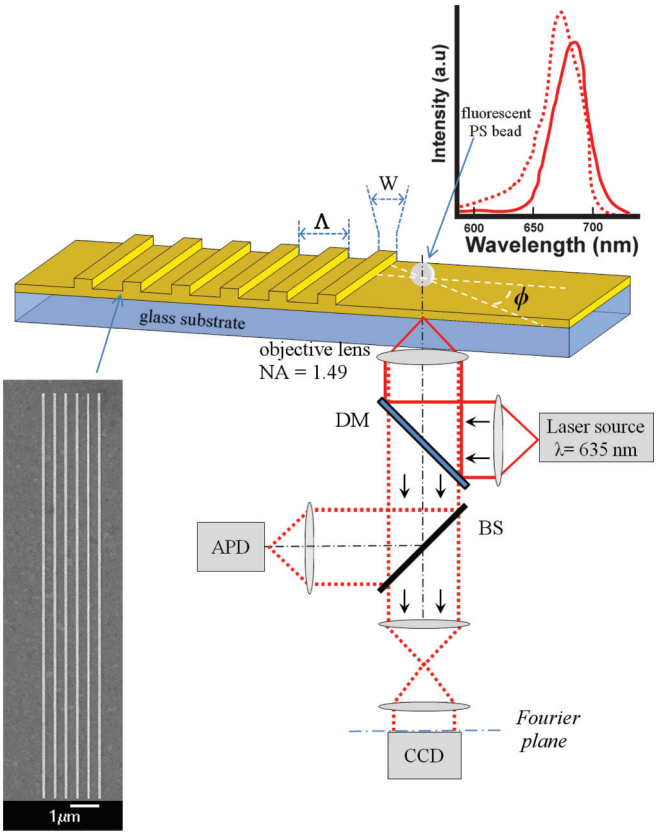

FIG. 1. (Color online) Scheme of SPCE leakage radiation microscopy. Fluorescent polystyrene (PS) nanobeads are excited using a 635 nm picosecond pulsed diode laser (LDH-P-635, Picoquant GmbH). The top inset depicts the absorption (dotted red curve) and emission (solid red curve) spectrum (Ref. 18) of the doped beads. Their fluorescence signal is filtered using a dichroic mirror and a 665 nm long-pass filter. A portion of the fluorescence signal is detected by an APD for scanning confocal microscopy. The rest is recorded in the Fourier plane with a CCD camera. DM: Dichroic mirror. BS: Beam splitter. APD: Avalanche photodiode. CCD: Charge coupled device camera (Andor Technology, Luca S 658M). Bottom inset: Scanning electron micrograph of a plasmonic DBR.

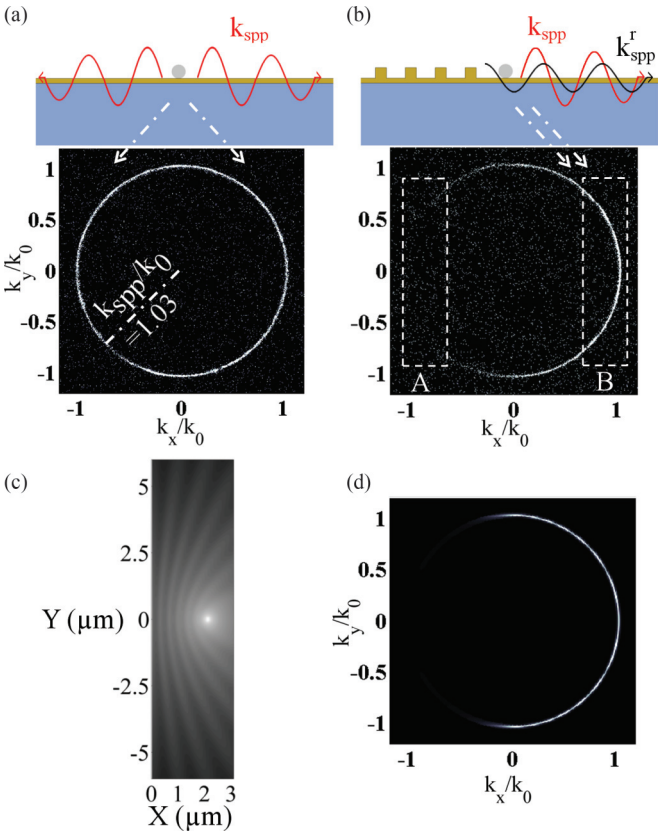

FIG. 2. (Color online) (a), (b) Radiation leakages of the fluorescent signal emitted by the PS nanobead recorded in the Fourier plane. In (b), the bead is in front of the mirror whereas it lies on a flat gold film in (a). The drawings on the top depict the SPP propagation. $\mathbf{k}_{SPP}$ and $\mathbf{k}^r_{SPP}$ refer to the incident and reflected wave vectors, respectively, and the corresponding SPP propagation towards and away from the plasmonic mirror are indicated by zones A and B in (b). (c), (d) Modeling of the image [(c), logarithmic scale] and Fourier (d) planes. The fluorescent source is located at 2.1 μm to the mirror.

the scanning electron micrograph in the inset) implemented onto a 50 nm thick gold film. Fabrication of this device is described in detail in Ref. 8. We spin-coated an aqueous suspension of fluorescent polystyrene particles (FS02F, Bang Laboratories, Inc.; mean diameter 60 nm) onto the sample. The nanobeads have an emission wavelength $\lambda_{em} = 690$ nm (see the spectrum in the inset of Fig. 1). We first imaged the randomly deposited nanoparticles by confocal scanning microscopy with a high numerical aperture (NA = 1.49, 100× oil immersion objective) in order to locate fluorescent beads of interest. SPCE is then analyzed by leakage radiation microscopy (LRM) in the Fourier plane as described in Ref. 21.

For a fluorescent bead located on a gold surface, the SPCE displayed in Fig. 2(a) shows a well-defined effective index $n_{SPP} = k_{SPP}/k_0 = 1.03 \pm 0.01$, in agreement with the calculated one ($n_{SPP} = k_{SPP}/k_0 = 1.034$). This first result indicates that the fluorescent bead composed of randomly oriented dye molecules acts as a local isotropic SPP source convenient for investigating the properties of the Bragg mirrors. The recorded signal is different when the bead is located in front of the Bragg mirror as shown in Fig. 2(b). Indeed, SPP wave vectors oriented towards the mirror are suppressed whereas the addition of the direct and reflected SPP waves leads to a brighter lobe in the opposite direction. We confirm that this SPCE distribution originates from reflection on the mirror with a simple model. To this aim, the isotropic SPCE from the fluorescent nanobead is described by a transverse magnetic (TM) field $\mathbf{H}(r) = H_0 e^{ik_{SPP}r} e^{-r/2L_{SPP}}/\sqrt{r}\mathbf{e}_\theta$, where $L_{SPP} = 10.5$ μm is the SPP propagation length calculated at $\lambda = 690$ nm. The plane mirror is modeled considering a secondary source, symmetric of the primary source with respect to the mirror plane and assuming an average reflection coefficient[22] $r = 0.2$. Figures 2(c) and 2(d) show the intensity distribution of the magnetic field $|\mathbf{H}(r)|^2$ and of its Fourier transform $|\widetilde{\mathbf{H}}(k_x,k_y)|^2$, respectively. The intensity of the Fourier-transform $|\widetilde{\mathbf{H}}(k_x,k_y)|^2$ calculated in Fig. 2(d) reproduces the experimental image recorded in the Fourier plane [Fig. 2(b)].

This confirms that the plasmonic mirror efficiently reflects the SPP launched by the fluorescent nanobead. Fourier-plane imaging also reveals that the mirror is efficient for incident angle $\phi \leqslant 40°$ [see the dark angular sector zone A in Fig. 2(b)], in agreement with a previous study.[23]

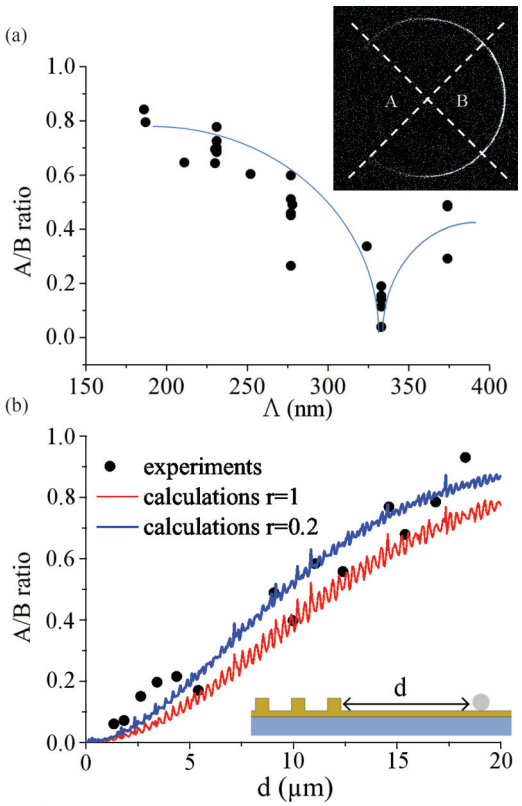

FIG. 3. (Color online) (a) Extinction ratio A/B as a function of the grating period (the solid line is a guide to the eyes). We have considered beads located at distance less than $d = 5\ \mu$m to the grating. (b) A/B as a function of the bead distance to grating for a fixed period $\Lambda = 333$ nm. Scattered points: experimental data, solid red curve: data calculated with Fourier planes simulated as done in Fig. 2(d) ($r = 0.2$). We also consider a perfect mirror ($r = 1$) to clearly see the interference oscillations.

Next, we investigate the effect of the grating period Λ. Figure 3(a) presents a figure of merit of the DBR. It is defined as the extinction ratio A/B where A and B refer to the SPP signal propagating towards and away from the mirror, respectively. Practically, A and B were estimated by integrating the intensity over the A and B areas indicated in the inset of Fig. 3(a). We observe an almost full extinction for $\Lambda = 333$ nm corresponding to half the SPP wavelength $\lambda_{SPP} = \lambda_{em}/n_{SPP} = 667$ nm, as expected for a SPP propagating at normal incidence. We also plot in Fig. 3(b) the A/B ratio as a function of the bead distance to the mirror. We observe that the extinction ratio decreases with the distance due to the finite SPP propagation length. The ratio A/B does not significantly change for distances $d \leqslant 5\ \mu$m between the bead and the grating, so that Fig. 3(a) is a measure of the mirror efficiency.

We plot in Fig. 3(b) the ratio A/B calculated using the simple model described above and achieve a good agreement with the measured data. We also consider a perfect mirror to clearly see the signal modulation. We check that the period of the small oscillations is $\lambda_{SPP}/2 = 333$ nm, due to interference between the forward and backward SPPs. We observe a large dispersion of the measured ratio A/B in Figs. 3(a) and 3(b) that may be explained by scattering on the gold ridges that is not taken into account in our simple model. The interference

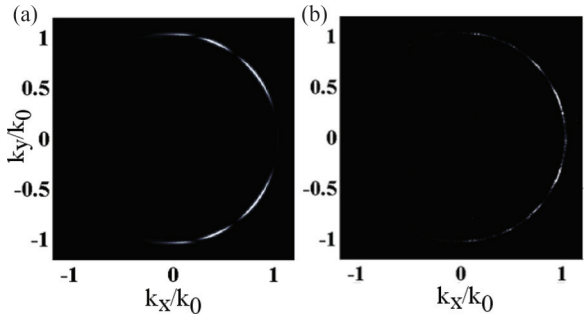

FIG. 4. (a) Simulated Fourier plane of a coherent source placed at 850 nm from a mirror with a reflection coefficient $r = 1$. (b) Fourier plane acquired for a fluorescent nanobead placed at 850 nm from a SPP Bragg mirror.

signature is also visible by close inspection of the image in the Fourier plane as observed in Fig. 4 since the optical path between the source and the mirror expresses $l = d/\cos(\phi)$. This reveals the spatial coherence of the localized nanosource.

The experimental results are further explained on the basis of the intrinsic properties of the Bragg mirror disregarding the local and incoherent nature of the SPP source. Indeed, Fig. 5(a) shows the reflectivity of a thin gold film textured by an infinitely extended Bragg mirror with parameters identical to the experimental ones. For a plane wave TM polarized with a plane of incidence perpendicular to the lines of the grating, the reflectivity reveals a broad band gap. The emission peak of our beads is located within this band gap, close to the upper band edge of the plasmonic Bloch mode sustained by the Bragg mirror. Indeed, the band gap width is $\Delta E \approx 0.27$ eV corresponding to free space wavelength range 675 nm $\leqslant \lambda \leqslant$ 790 nm. This covers the emission spectra of the fluorescent nanobeads (centered at $\lambda_{em} = 690$ nm and with a full width at half maximum FWHM ≈ 35 nm[18]). Next, we compute the isofrequency reflectivity map of the infinitely extended Bragg mirror at the free space wavelength of $\lambda_{em} = 690$ nm [see Fig. 5(b)]. We observe an acceptance angle of $\phi \leqslant 30°$

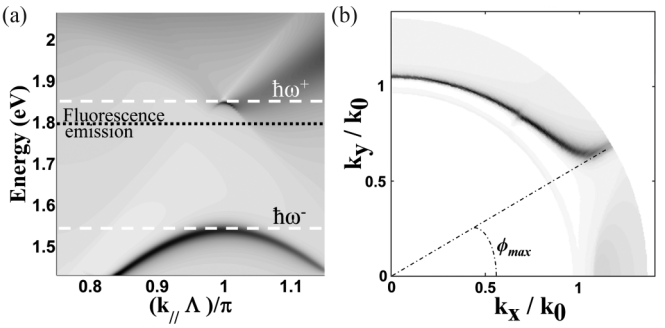

FIG. 5. (a) Calculated reflectivity R of a periodically textured film [gray scale from $R = 0.4$ (black) to $R = 1$ (white)]. The pitch of the grating is $\Lambda = 333$ nm. $\hbar\omega^+$ and $\hbar\omega^-$ denote the upper and the lower boundaries of the energy band gap opened by the textured film. They correspond to free-space wavelengths $\lambda^+ = 675$ nm and $\lambda^- = 790$ nm, respectively. The fluorescence emission frequency is within the band gap ($R = 0.86$ at fluorescence emission $\hbar\omega_{em} = 1.79$ eV). (b) Isofrequency map of the reflectivity computed at the fluorescence emission wavelength ($\lambda_{em} = 690$ nm).

in reasonable agreement with $\phi \leqslant 40^\circ$ obtained for the six ridges used experimentally. This demonstrates that the large bandwidth of plasmonic Bragg mirrors is adapted to control emission at room temperature. Relying on these results, we have designed in-plane cavities discussed in the next section.

III. IN-PLANE SPP CAVITY

A. Decay rate and relaxation channels

Let us now consider an in-plane SPP cavity opened between two plasmonic Bragg mirrors. We are interested in measuring the fluorescence lifetime of single molecules spread in the planar plasmonic cavity. In this part, we numerically investigate the fluorescence decay rate of single molecules placed in the plasmonic cavity, before the experimental measurements discussed in the next section. We selected high quantum efficiency dye molecules emitting at $\lambda_{em} = 670$ nm, close to the regime studied in the previous section.

The SPP effective index of a glass/gold (50 nm)/air slab is $n_{SPP} = 1.037$ at this wavelength. The distributed Bragg mirror period is therefore fixed at $\Lambda = \lambda_{em}/(2n_{SPP}) \approx 320$ nm. It consists of six 50 nm $\times$ 50 nm gold ridges. The fluorescence decay of a dipolar emitter is calculated with the formalism explained in Ref. 24. For simplicity, the emitter is located at the cavity center, 25 nm above the gold film.

To this aim, we first calculate the power $P(k_y)$ dissipated by a dipolar emitter as a function of the in-plane wave vector k_y along the invariant axis, as shown in Fig. 6 for a vertical dipole and in Fig. 7 for a horizontal dipole. These calculations

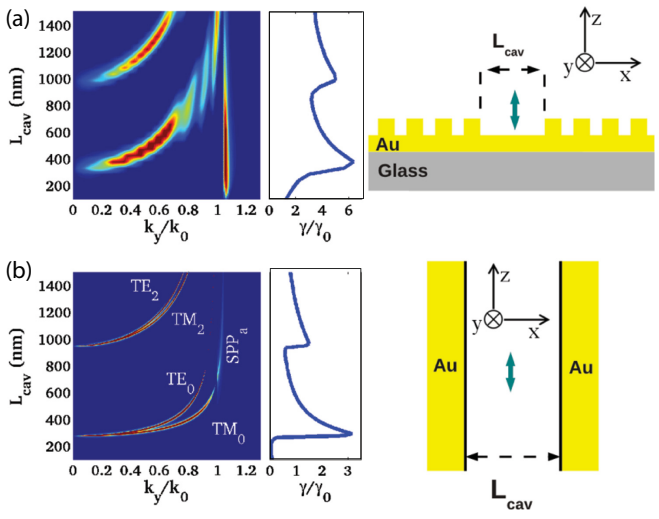

FIG. 6. (Color online) (a) Power dissipated by a dipolar emitter inside the plasmonic cavity, as a function of cavity length L_{cav} and in plane wave vector along the cavity axis k_y/k_0. The glass/gold/air slab contribution is subtracted to characterize the cavity effect. Inset: Decay rate as a function of the cavity length obtained by integrating the dissipated power over all the k_y/k_0 spectrum range (including the glass/gold/air slab contribution). (b) Same as (a) for a 1D gold/air/gold cavity. The dipolar emitter is located at the cavity center and parallel to the mirror walls. The 1D cavity modes are indicated on the dispersion curve. SPP$_a$ and SPP$_b$ [see Fig. 7(b)] are gap plasmons resulting from the coupling between the gold/air SPP supported by the two mirrors (note that the photonic guided TM$_0$ mode continuously evolves to the gap plasmon SPP$_a$ when the cavity size increases) (Ref. 25).

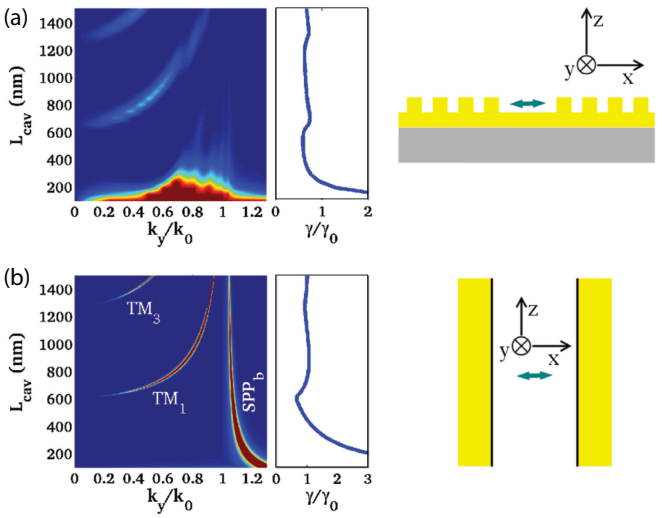

FIG. 7. (Color online) Same as Fig. 6 for a dipolar emitter perpendicular to the mirror walls.

are performed by numerically evaluating the 2D Green's dyad associated with the cavity.[24,26–28] In order to focus on the role of the cavity on the emission process, we subtracted the glass/gold/air slab contribution (no grating). For a given cavity size L_{cav}, the main contribution to the dissipated power appears at a given wave vector k_y, associated with a cavity mode. Thus the dissipated power is strongly increased by coupling to the cavity modes, as expected. The total decay rate at the center of the cavity is then computed by integrating the dissipated power over the whole wave vector spectrum for each cavity size [see the insets of Figs. 6(a) and 7(a)]. Recalling that the SPP wavelength is $\lambda_{SPP} = \lambda_{em}/n_{SPP} = 645$ nm, we observe that the fluorescence decay rate increases for cavity length in close proximity to odd multiples of $\lambda_{SPP}/2$. Precisely, following Ref. 8, the dispersion relation of the cavity opened between two Bragg mirrors is better described as a function of the parameter $\delta = L_{cav} - \Lambda + W$ representing the excess of size of the cavity as compared to the mirror period. We check that new cavity modes appear for $\delta \approx (2k+1)\lambda_{SPP}/4$ with $k = 1,2,\ldots$, as expected.

It is interesting to compare the behavior of the in-plane plasmonic cavity to a one-dimensional (1D) metal/insulator/metal cavity,[29–31] as presented in Fig. 6(b). We observe strong similarities since the plasmonic cavity confines a surface wave in direct analogy with a 1D optical microcavity that confines a bulk wave. The difference is that the SPP is naturally confined near the metal surface, whereas the 1D modes are delocalized along two directions.

The largest emission rate enhancements are observed for a dipolar emitter oriented parallel to the mirrors, i.e., perpendicular to the slab surface, in agreement with the SPP polarization (Fig. 6). It occurs due to the emission coupling to even cavity modes, namely TM$_0$/TE$_0$ and TM$_2$/TE$_2$ in the 1D cavity[29,31] and their plasmonic counterparts in the planar cavity. These modes present an antinode at the cavity center so that they are efficiently excited by the dipolar emitter. Note that only one polarization is allowed in the SPP cavity since it confines the polarized SPP sustained by the substrate/gold/air

slab (TM polarized with respect to the slab orientation, that is, E_z electric field corresponding to TE mode of the 1D cavity). A dipolar emitter oriented perpendicular to the mirrors couples weakly to odd cavity modes so that it results in a weak modification of its decay rate, except for small cavity sizes (Fig. 7). Although we observe similar behaviors at short cavity length for a dipole coupled to 1D and planar cavities, it comes from different processes. In a 1D cavity, the coupling originates from a large *nonradiative* transfer to the gap plasmon SPP_b leading to a fluorescence quenching. Differently, we observe a strong power dissipation spanning a large wave vector range in the plasmonic case [Fig. 7(a)]. This indicates an efficient scattering of the plasmon field by the ridges leading to an increase of the *radiative* rate. Note that this occurs around $0.6 \leqslant k_y/k_0 \leqslant 1$ corresponding to the angular range for which the reflectors are inefficient as seen in Fig. 4(b). The peak near $L_{cav} \approx 270$ nm (corresponding to full grating condition $\delta = 0$) and $k_y/k_0 = 0.6$ is related to the particular point in Fig. 4(b) below which no Bloch mode is supported. Last, we observe a very weak decay rate modification for a dipolar emitter oriented along the y axis (not shown).

B. Single-molecule fluorescence lifetime imaging

Figure 8 depicts the setup used for scanning confocal fluorescence lifetime imaging (confocal FLIM) of single molecules spread into a plasmonic cavity. Dye molecules (DiD, Invitrogen, $\lambda_{em} = 670$ nm) were dispersed in a polymethyl methacrylate (PMMA, toluene solvent) solution at a nanomolar concentration. A 35 nm thick dye-doped PMMA film is then spin-coated on the plasmonic cavity. Prior to the dye-doped polymer matrix, a 30 nm thick SiO_2 film was deposited by plasma sputtering. This spacer avoids fluorescence quenching near the gold film. Each distributed Bragg mirror consists of six gold ridges (width $W = 140$ nm, height $h = 50$ nm) periodically separated by $\Lambda = 250$ nm. This period was taken as the half SPP wavelength of the glass/gold(50 nm)/SiO_2(30 nm)/PMMA(35 nm)/air multilayer system ($n_{SPP} = 1.27$, $\lambda_{SPP} = 526$ nm at the emission wavelength $\lambda_{em} = 670$ nm).

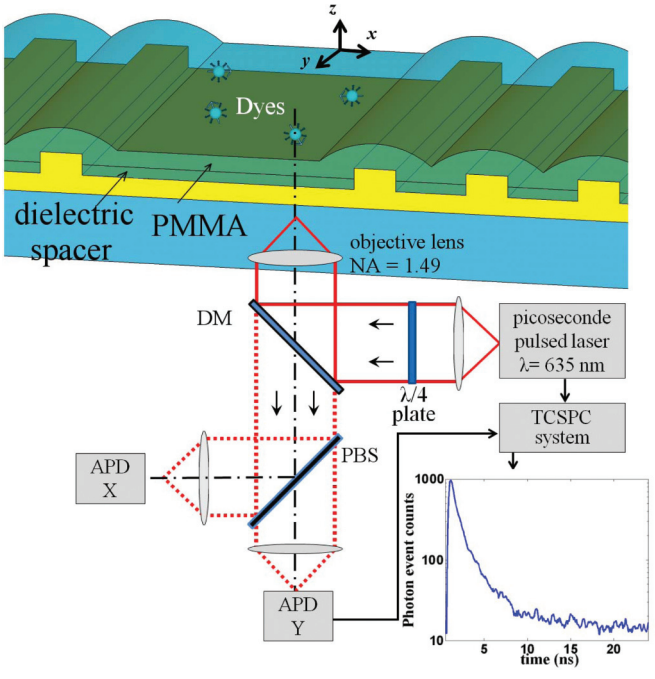

FIG. 8. (Color online) Confocal FLIM setup. Dye molecules randomly deposited into a plasmonic cavity are excited with a circularly polarized laser beam. Fluorescence emission is divided by a polarized beam splitter (PBS) and collected on two APDs (Excelitas Technologies SPCM-AQRH-15). APD-Y is connected to a time-correlated single photon counting card (TCSPC; Picoquant-PicoHarp 300) for fluorescence decay acquisition (inset).

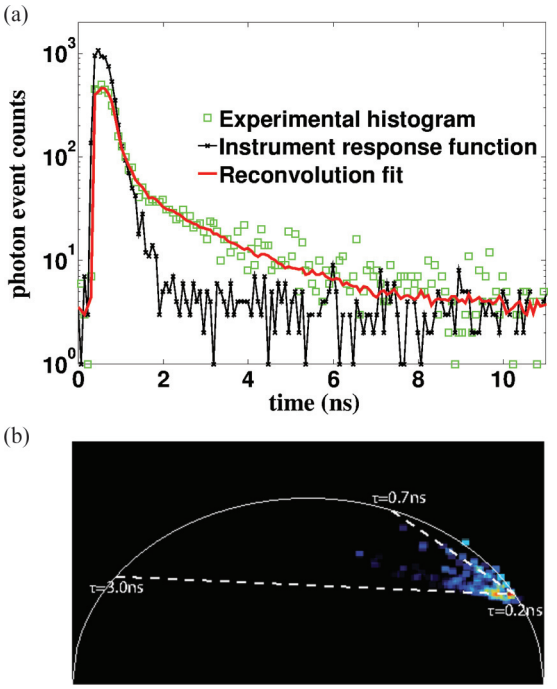

FIG. 9. (Color online) (a) Green scattered points: TCSPC histogram recorded for a single dye inside a cavity. Black curve: Instrument response function (IRF) of the microscope. Red curve: Result of the reconvolution fitting procedure. (b) Polar representation of the fluorescence lifetime. Each point refers to a single-molecule lifetime measurement. The right part of the figure corresponds to short lifetimes whereas the left part corresponds to long lifetimes.

Single-molecule detection is performed using the same home-built scanning confocal microscope described in the first section. We added a $\lambda/4$ wave plate in order to excite the fluorescent molecules with a circularly polarized light. Therefore all in-plane and out-of-plane oriented dye molecules are efficiently excited. The x- and y-polarized photoluminescences are detected on two different APDs, leading to two simultaneous image acquisitions. The x-polarized signal detected on the APD-X records the gold photoluminescence background signal used to locate the position of the grating since the signal is enhanced at the ridges.[32] Last, we measured the fluorescence lifetime of individual molecules as a function of the cavity size and the molecule position into the cavity.

Figure 9 shows a time-correlated single-photon count (TCSPC) histogram (green scatter) recorded from a single dye located inside a cavity. The instrument response function (IRF) of the microscope (black curve) is used for a

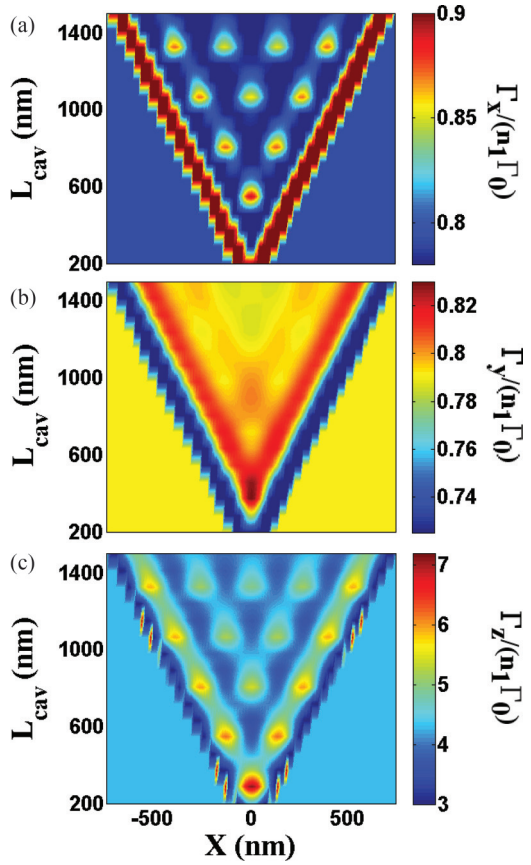

FIG. 10. (Color online) (a), (c) Normalized fluorescence decay rate as a function of cavity size L_{cav} and molecule position for x- (a), y- (b), and z- (c) oriented emitter. Decay rates are normalized with respect to their value $n_1\Gamma_0$ in a homogeneous background of optical index n_1. The value outside the cavity refers to the decay rate in absence of the gold gratings.

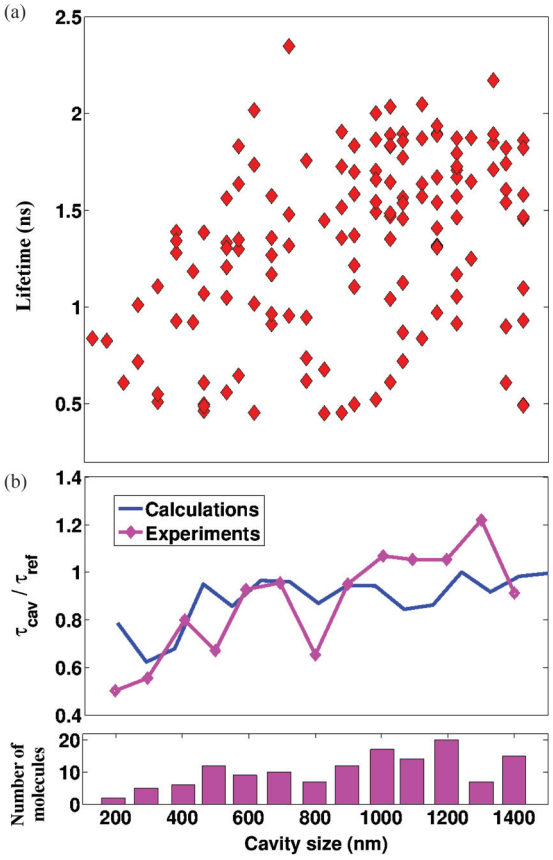

FIG. 11. (Color online) (a) Fluorescence lifetime as a function of the cavity size. (b) Average lifetime as a function of the cavity size (purple curve). The blue curve is calculated assuming a mean molecule position $z = 25$ nm above the metal film. Lifetimes are normalized with respect to the reference measured ($\tau_{ref} = 1.43$ ns) or calculated ($\tau_{ref}/\tau_0 = 0.51$) far from the cavity. The bottom panel depicts the number of considered molecules for each cavity size.

biexponential reconvolution fitting procedure to evaluate the lifetime trace (red curve). The small lifetime component (dozens of picoseconds) is attributed to the background signal,[33] notably gold photoluminescence. The long-lifetime component corresponds to the fluorescence lifetime of the dye molecule. The FWHM of the IRF histogram is measured to 450 ps and defines the lower limit for lifetime measurement. Overall, we have measured the fluorescence lifetime of 137 molecules randomly spread into plasmonic cavities with length ranging from 200 nm to 1.4 μm. Since the gold photoluminescence makes difficult the measurement of the lifetime, we cross-check our measurement using a polar representation [see Fig. 9(b)]. In this representation, each point is defined by its (u,v) coordinates which are the cosine and sine transforms of the fluorescence intensity decay.[34] Single-exponential decays are located on the semicircle with long lifetime on the left and short lifetime on the right of the circle. In the case of biexponential behavior, as here, each measurement is represented by a point inside the semicircle. By plotting a line that joins the experimental measure and short lifetime, we can estimate the long fluorescence lifetime and the respective contribution of each component. This method avoids any fitting procedure and leads to robust evaluation of the lifetimes. In the present case, we observe an important contribution of the short lifetimes but we confirm the value achieved using a standard fitting procedure with fluorescence lifetime ranging from 0.7 ns to 3 ns. Note that the polar representation and fitting procedure are independent methods. Finally, we estimate the errors on the measured fluorescence lifetime to 200 ps.

The photodynamic of individual dye molecules located into a planar cavity depends on several parameters, namely their orientation, position (distance to the mirror but also altitude), and the length of the cavity. In the following, we try to identify the main trends. To this purpose, we compare the measured lifetime to numerical simulations. Practically, we considered two distributed Bragg mirrors made of 6 gold ridges ($W = 130$ nm, $h = 50$ nm, $\Lambda = 250$ nm) deposited on a 50 nm thick gold film and supported on a glass substrate. The main difference is related to the multilayer system used in the simulation. In order to keep the computing time reasonable, we consider three layers, namely glass/gold(50 nm)/effective medium where the effective medium has an optical index fixed to $n_1 = 1.2$ since it leads to a similar SPP effective index $n_{SPP} = 1.27$ as the glass/gold/SiO_2/PMMA/air multilayer system. The SPP propagation length is however underestimated

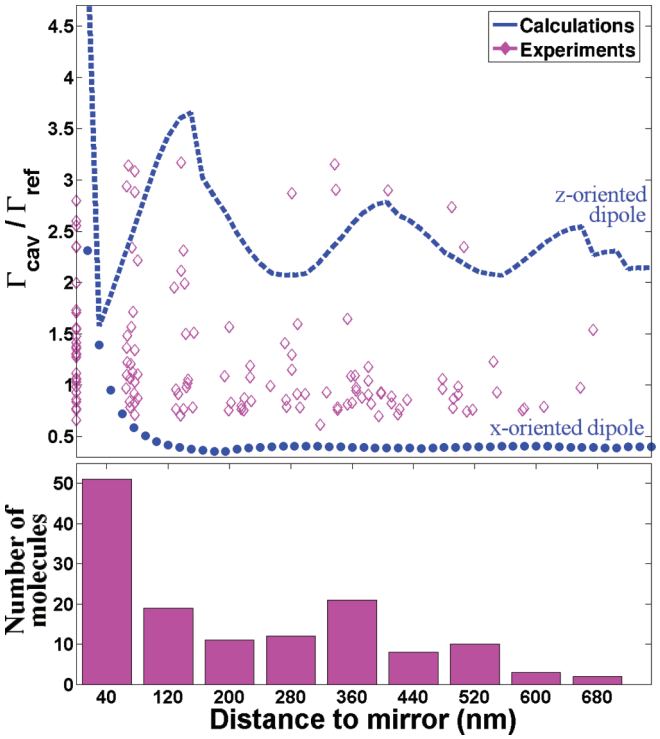

FIG. 12. (Color online) Distribution of the fluorescence decay rate as a function of distance to the closest Bragg mirror for all cavity sizes (purple diamonds). The dotted (dashed) curve is the minimum (maximum) calculated decay rate for an x-oriented (z-oriented) dipole.

using this effective medium ($L_{spp} = 1.9\ \mu$m instead of $L_{spp} = 5\ \mu$m). In first approximation, this difference can be safely disregarded since we demonstrated recently that the surface plasmon coupled emission rate does not depend on the propagation length.[24,35] We considered a dipolar emitter 25 nm above the gold film.

Figure 10 shows the decay rate calculated as a function of cavity size and molecule position for three emitter orientations. We observe oscillations typical from coupling to the cavity modes, already observed in a 1D cavity.[31] As already pointed out, the largest decay rates are obtained for a vertical emitter.

Figure 11(a) shows the measured lifetimes as a function of the cavity size. The dispersion of the measurements is due to both the position and the orientation of the dye molecules. 75 more measurements were also performed for molecules far from the cavities (i.e., embedded in the PMMA matrix within the glass/gold/SiO_2/PMMA/air multilayer system) and are taken as reference measurements. The calculated reference lifetime is $\tau_{ref}/\tau_1 = 0.51$ in agreement with the experimental one estimated to $\tau_{ref}/\tau_1 = 1.43/2.6 = 0.55$, where $\tau_1 = 2.6$ ns was measured in a PMMA matrix.[31] In the following, fluorescence lifetimes are normalized with respect to the average reference lifetime to focus on the plasmonic cavity role. In Fig. 11(b), we compare the measured and calculated lifetimes. In order to assess a first trend, we averaged the lifetimes for each cavity size. The experimental curve is in qualitative agreement with the calculated one with variations related to the coupling to cavity modes. We also plot the normalized

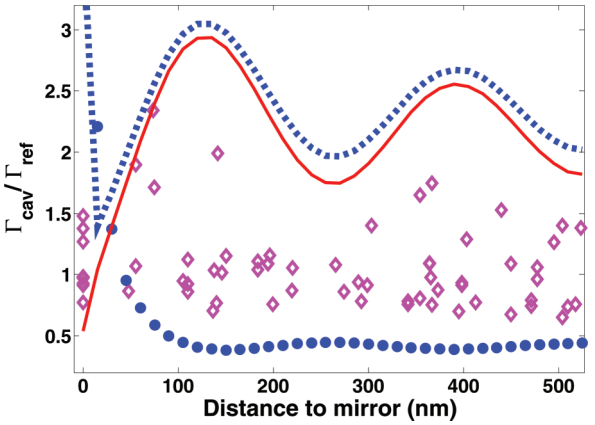

FIG. 13. (Color online) Measured normalized decay rates as a function of distance to the closest mirror for a cavity length $L_{cav} = 1.1\ \mu$m (purple diamonds). Decay rates calculated for a z-oriented (dashed curve) and an x-oriented (dots) dipole are also shown. The calculated radiative decay is plotted for a z-oriented emitter (solid red curve).

decay rate ($\Gamma_{cav}/\Gamma_{ref} = \tau_{ref}/\tau_{cav}$) distribution as a function of the molecule's distance from the mirror in Fig. 12. We observe large dispersion of the measured decays for a given distance to the mirror since resonant and nonresonant cavity lengths are involved. We also represent the maximum and minimum decay rates expected for a z- and x-oriented dipole, respectively. This qualitatively reproduces the measured lifetime dispersion. The small discrepancies are attributed to the simplifications used in our model.

Figure 13 presents the evolution of the decay rate as a function of the position inside a resonant 1.1 μm cavity. The observed dispersion is again in agreement with the numerical simulations. Maximum decay rate enhancement is $\Gamma/\Gamma_{ref} = 2.3$ as compared to a flat gold film. This corresponds to an enhancement factor (Purcell factor) of $F_P = \Gamma/n_1\Gamma_0 = 2.3/0.5 = 4.5$. It could reach $F_p \approx 7$ in a single mode cavity [see Fig. 10(c)]. This reveals the capability of a planar plasmonic cavity to control fluorescent emission. Finally, we calculate the radiative contribution to the total decay rate (red dashed curve) since light extraction is an important aspect to consider.[12] This is estimated by vanishing the imaginary part of the dielectric function of gold. We estimate the quantum efficiency to $\Gamma_{rad}/\Gamma_{tot} \approx 0.9$ so that high extraction efficiency is expected from such planar plasmonic cavity. This originates from SPP decoupling into the substrate.[24] However, the radiative contribution cancels near the mirror since nonradiative energy transfer to the metal dominates.

IV. CONCLUSION

To summarize, we have demonstrated at the single-molecule level that a plasmonic planar cavity permits emission control thanks to surface wave confinement. This is in direct analogy to fluorescence emission governed by bulk mode confinement in an optical dielectric microcavity. We first studied the effect of SPP mirrors on surface plasmon coupled emission by leakage radiation microscopy. We have

demonstrated that the mirrors remain efficient when excited by a localized SPP source at room temperature. Then, we measured the fluorescence lifetime into in-plane SPP cavities and interpreted the modifications with the help of numerical simulations. This leads to a clear understanding of the role of the cavity modes in the emission mechanism. We estimated a high decay rate enhancement (up to 7 in a $\lambda_{SPP}/2$ cavity for a z-oriented dipole). Finally, we have shown that efficient radiation decoupling of the SPP into the substrate leads to high apparent quantum yield of great interest for light extraction. Thus, profiting of both SPP confinement and leakage, we were able to design a simple cavity that leads to an efficient emission enhancement and extraction by direct coupling to a surface mode. This would be very helpful for improving solid state light emitting diodes. As an added value, let us also note that the emitters located inside the SPP cavity are accessible for external manipulation with, e.g., optical tweezers or an AFM tip.

ACKNOWLEDGMENTS

This work is supported by the Agence Nationale de la Recherche (contract QDOTICS ANR-12-BS10-008). A.K. acknowledges a grant from the Regional Council of Burgundy under the PARI-SMT3 program. Calculations were performed using DSI-CCUB resources and samples were realized using ARCEN nanofabrication facilities.

*gerard.colas-des-francs@u-bourgogne.fr

[1] T. Benson *et al.*, in *Frontiers in Planar Light-Wave Circuit Technology*, edited by S. Janz, J. Ctyroky, and S. Toyan (Springer, Berlin, 2006), pp. 39–70.
[2] S. Bär *et al.*, Anal. Bioanal. Chem. **396**, 3 (2010).
[3] K. Busch *et al.*, Phys. Rep. **444**, 101 (2007).
[4] J. Foresi *et al.*, Nature (London) **390**, 143 (1997).
[5] A. Koenderink *et al.*, Photonics and Nanostructures: Fundamentals and Applications **3**, 63 (2005).
[6] C. Renaut, B. Cluzel, J. Dellinger, L. Lalouat, E. Picard, D. Peyrade, E. Hadji, and F. de Fornel, Sci. Rep. **3**, 2290 (2013).
[7] E. Descrovi, V. Paeder, L. Vaccaro, and H.-P. Herzig, Opt. Express **13**, 7017 (2005).
[8] J.-C. Weeber *et al.*, Nano Lett. **7**, 1352 (2007).
[9] J. C. Weeber, A. Bouhelier, G. Colas des Francs, S. Massenot, J. Grandidier, L. Markey, and A. Dereux, Phys. Rev. B **76**, 113405 (2007).
[10] S. Z. Q. Wang and J. Wang, Opt. Express **16**, 19882 (2008).
[11] Y. Gong *et al.*, Appl. Phys. Lett. **94**, 013106 (2009).
[12] I. Mallek-Zouari *et al.*, Appl. Phys. Lett. **97**, 053109 (2010).
[13] G. Di Martino *et al.*, Nano Lett. **12**, 2504 (2012).
[14] N. de Leon and M. Lukin, IEEE J. Sel. Top. Quantum Electron. **18**, 1781 (2012).
[15] M. Kuttge, E. J. R. Vesseur, and A. Polman, Appl. Phys. Lett. **94**, 183104 (2009).
[16] M. Honda and N. Yamamoto, Opt. Express **21**, 11973 (2013).
[17] G. Winter, W. A. Murray, S. Wedge, and W. L. Barnes, J. Phys.: Condens. Matter **20**, 304218 (2008).
[18] See http://www.bangslabs.com.
[19] I. Gryczynski, J. Malicka, Z. Gryczynski, and J. R. Lakowicz, J. Phys. Chem. B **108**, 12568 (2004).
[20] D. G. Zhang, X.-C. Yuan, and J. Teng, App. Phys. Lett. **97**, 231117 (2010).
[21] J. Grandidier *et al.*, J. Microsc. **239**, 167 (2010).
[22] M. U. Gonzalez, J. C. Weeber, A. L. Baudrion, A. Dereux, A. L. Stepanov, J. R. Krenn, E. Devaux, and T. W. Ebbesen, Phys. Rev. B **73**, 155416 (2006).
[23] M. U. Gonzàlez *et al.*, Opt. Lett. **32**, 2704 (2007).
[24] J. Barthes, G. Colas des Francs, A. Bouhelier, J. C. Weeber, and A. Dereux, Phys. Rev. B **84**, 073403 (2011).
[25] E. Feigenbaum and M. Orenstein, J. Light. Tech. **25**, 2547 (2007).
[26] G. Lévêque and O. Martin, J. Appl. Phys. **100**, 124301 (2006).
[27] G. Colas des Francs, J. Grandidier, S. Massenot, A. Bouhelier, J. C. Weeber, and A. Dereux, Phys. Rev. B **80**, 115419 (2009).
[28] R. Marty, C. Girard, A. Arbouet, and G. Colas des Francs, Chem. Phys. Lett. **532**, 100 (2012).
[29] P. T. Worthing, J. A. E. Wasey, and W. L. Barnes, J. Appl. Phys. **89**, 615 (2001).
[30] M. Steiner *et al.*, New J. Phys. **10**, 123017 (2008).
[31] J. P. Hoogenboom *et al.*, Nano Lett. **9**, 1189 (2009).
[32] H. Kim *et al.*, J. Phys. Chem. C **112**, 12721 (2008).
[33] M. Patting, *Practical TCSPC Data Analysis, in 8th European Short Course on "Principles and Applications of Time-Resolved Fluorescence Spectroscopy"* (http://www.picoquant.com/events/details/fluorescence-course-2010, Berlin, 2010).
[34] A. Leray *et al.*, J. Microsc. **248**, 66 (2012).
[35] J. Barthes, A. Bouhelier, A. Dereux, and G. Colas des Francs, Sci. Rep. **3**, 2734 (2013).